

Effects of One-step and Two-step Treatment Regimes on the Characteristics of Plasma Electrolytic Oxidation (PEO) Coatings on Aluminum

Ye-kang Wu¹, Hui-ping Han¹, Rui-qiang Wang², Guo-rui Wu^{1,3}, Xu-zhen Zhang¹, Yu Su¹, Da-long Li⁴, Chang-hong Guo⁴, Sheng-xue Yu¹, De-jiu Shen^{1,*}, Philip Nash⁵

¹ State Key Laboratory of Metastable Materials Science and Technology, College of Materials Science and Engineering, Yanshan University, Qinhuangdao 066004, PR. China

² School of Material Science and Engineering, Beijing Institute of Technology, Beijing 100081, PR. China

³ CITIC Dicastal Limited by Share Ltd, Qinhuangdao 066000, PR. China

⁴ College of Mechanical Engineering, Yanshan University, Qinhuangdao 066004, PR. China

⁵ Thermal Processing Technology Center, Illinois Institute of Technology, Chicago, IL 60616, USA

*E-mail: DejiuShen@163.com

Received: 25 November 2018 / Accepted: 25 January 2019 / Published: 10 April 2019

Plasma electrolytic oxidation (PEO) processing of aluminum is galvanostatically carried out through one-step and two-step treatment regimes in an alkaline sodium silicate electrolyte without and with sodium tungstate additive agent. The microstructure, phase composition and corrosion resistance of the resultant coatings are investigated by means of scanning electron microscopy (SEM), X-ray diffraction (XRD), 3-dimensional imaging techniques and potentiodynamic polarization tests. Some PEO coatings are stripped from the aluminum substrate via an electrochemical coating stripping method to intuitively disclose the corresponding relations among the characteristic structures of the free surface, fractured cross-section and coating/substrate interface. Further, coating growth models describing the one-step and two-step treatments are proposed according to the present PEO coating microstructure characteristics. The potentiodynamic polarization test results demonstrate that the one-step PEO coating treated in the compound silicate-tungstate electrolyte for 20 min exhibits the best resistance to corrosion as compared to bare Al and other PEO coatings.

Keywords: Plasma electrolytic oxidation; Treatment regime; Stripped coating; Microstructure corresponding relation; Growth model

1. INTRODUCTION

Plasma electrolytic oxidation (PEO) is a novel surface modification technique, through which protective ceramic-like coatings can be in situ fabricated on valve metals (Al, Mg, Ti, Zr, V, Ta, Nb,

etc.) in associated electrolyte systems [1, 2]. The resultant ceramic coatings usually possess excellent performance, such as corrosion, wear and thermal resistances [1, 3-6]. The PEO technique evolved from conventional anodizing, but it is usually carried out at a higher applied voltage range, which leads to a much more complex reaction process relative to that of conventional anodizing. Therefore, a great number of studies have been devoted to the investigation of PEO processes. To date, considerable and significant progress has been made in the essential characteristics of PEO processes by means of a variety of effective research methods, such as optical, electrical, acoustic, frequency response, electrochemical impedance spectroscopy and tracers [3, 5, 7-13]. Currently, it is obvious that the non-linear time-variant PEO process involves not only chemical and electrochemical reactions but also thermochemical and plasma-chemical reactions, accompanied by gas liberation, acoustic activity, luminous emission, dielectric breakdown and plasma discharge [5]. However, there is still much research to be done to further investigate the growth mechanisms of PEO coatings under different treatment conditions and regimes.

In the characterization and analysis of PEO-related studies, the cross-sectional observations of commonly mounted specimens are involved in most cases during SEM examinations to exhibit the coating microstructure characteristics. However, it is usual that the cross-sectional microstructures of PEO coatings are locally distorted or metamorphosed in the wearing/polishing process used to prepare the cross-section specimens, so some unreal cross-sectional microstructures of the coatings have been observed to some extent. In recent decades, to gain insight into the real cross-sectional microstructures and coating/substrate interfaces of PEO coatings, the epoxy replica method [14], tomography imaging techniques [15-18] and coating stripping means (chemical- [15, 19-21] and electrochemical-related [22-30]) have been employed by researchers. Among these means, the electrochemical stripping of PEO coatings on Al and its alloys has gradually received good graces due to its low cost, neutral media, simple operation and desirable outcome. After a coating was stripped from the underlying aluminum substrate through an electrochemical stripping method [22-26], our research team performed multi-angle observations on the stripped PEO coatings, and some new and interesting features of the cross-section and coating/substrate interface were discovered. Likewise, by adopting this method, Zou and coauthors [28] observed free-standing stripped PEO coatings combined with the correlative microdischarge-sculpted aluminum base, and they further established the connection between the individual pulse energy and the 'local over-growth' characteristic across the coating/substrate interface. Sabouri and coauthors [27] prepared electrochemically-stripped PEO coatings to investigate the effect of multiwall carbon nanotubes (MWCNTs) on the morphology and corrosion behavior of the produced Al-based PEO coatings, and investigations of the cross-sections and the coating/substrate interfaces of the stripped coatings were conducted.

So far, as an item of vital content, the role of the two-step PEO treatment, which is used on various valve metals and in diverse acidic and alkaline electrolytes, has been increasingly addressed [1, 31-34]. This treatment mode is not only applied to study the formation mechanisms of the corresponding PEO coatings [32, 33], but also to examine the effects of PEO treatment conditions, such as electrolyte constituents and electrical characteristics, on the microstructures, compositions and performances [1, 31, 34, 35]. In the present study, the effects of one-step and two-step treatments on the microstructure and corrosion resistance of PEO coatings on Al in an alkaline silicate electrolyte

system without and with tungstate addition were investigated. Particularly, some PEO coatings were stripped from the Al substrate via an electrochemical approach with the aim of disclosing the corresponding relationships of the characteristic microstructures among the free surface, fractured cross-section and coating/substrate interface, which can provide an efficient way to establish growth models for the present coatings elaborated via one-step and two-step treatment regimes.

2. EXPERIMENTAL

2.1. Materials and PEO coating process

Specimens of 99.6% aluminum foil with dimensions of 15 mm×15 mm×0.2 mm were used as the substrates for PEO experiments. Prior to each PEO treatment, the as-received bare Al specimen was ultrasonically cleaned in acetone and then in ethanol, followed by being dried at normal temperature and pressure. The PEO process was conducted using a self-developed PEO power supply with heteropolar asymmetric pulses, and the bare Al specimen and the stainless-steel reservoir (4 liters) functioned as the anode and cathode, respectively. As shown in Table 1, an alkaline sodium silicate electrolyte (referred to as Si) and the basic electrolyte with sodium tungstate addition (referred to as SiW) were used in this study. The associated electrochemical properties (pH and conductivity) of the two transparent viscous electrolytes were listed in Table 1. All the electrolytic solutions were prepared with analytical grade reagents and deionized water.

Table 1. Electrolyte components and the associated electrochemical properties (18.0°C)

Code	Electrolyte constituents	pH	Conductivity (mS/cm)
Si	2 g/l NaOH+8 g/l Na ₂ SiO ₃ •9H ₂ O	13.10	12.39
SiW	2 g/l NaOH + 8 g/l Na ₂ SiO ₃ •9H ₂ O +8 g/l Na ₂ WO ₄ •2H ₂ O	12.96	14.10

One-step and two-step PEO treatment regimes were adopted in the present work according to the treatment conditions shown in Table 2. Primary coatings of P1 and P2 were included in the experimental scheme to investigate the effect of the inevitable intermediate results (precursor coatings) on the microstructural evolution of one-step and two-step PEO treatments. Clearly, P1 is the primary coating of OS1 and TS1; Similarly, P2 is the primary coating of OS2 and TS2. During the coating process, the electrical parameters employed, including the current density, frequency, duty ratio and positive-to-negative pulse length ratio, were fixed at 22 mA/cm², 50 Hz, 50%, and 5/1, respectively. The galvanostatic dependence of the applied positive voltage upon the PEO treatment time was recorded and converted using the LabView data acquisition system (National Instruments, USA) with a sampling frequency of 10³ Hz.

Table 2. PEO treatment conditions of Al specimens.

Specimen code	PEO treatment conditions
P1	Treated in Si for 10 min
P2	Treated in SiW for 10 min
OS1	Treated in Si for 20 min
OS2	Treated in SiW for 20 min
TS1	Treated firstly in Si for 10 min and then in SiW for 10 min
TS2	Treated firstly in SiW for 10 min and then in Si for 10 min

Note: “P”, “OS” and “TS” are the abbreviation of “primary”, “one-step” and “two-step”, respectively.

For all PEO treatment conditions, a cooling system and an agitator were employed to ensure that the temperature of the electrolyte was less than 35°C. Both the stirring speed of the agitator and the position of the anode remained constant to guarantee data consistency. After the PEO process, the coated Al specimens were successively rinsed with running tap water and distilled water, and then dried in warm air.

2.2. Stripping of PEO coatings

Some PEO coatings synthesized under the aforementioned PEO treatment conditions in the current-controlled mode were stripped from the underlying uncoated aluminum substrate via a patent technology involving an electrochemical method [36]. The equipment employed and the procedure operations for the coating stripping have been described in detail in our previous studies [22, 24]. After completing the stripping procedure, the stripped PEO coatings were immersed into distilled water for 12 h and then naturally air-dried in the lab. Two sets of stripped coatings from the Al specimens obtained under the identical PEO experimental parameters were prepared: the first set displayed a fractured cross-section of the stripped coatings, and the second presented a coating/substrate interface which was directly adjacent to the metallic base, i.e., the backsides of the stripped coatings.

2.3. Specimen characterizations

The phase components of the as-prepared PEO coatings were identified by X-ray diffractometry (XRD, D/Max-rB, Rigaku, Japan) with Cu K α radiation, and the scan was operated at 40 kV and 100 mA in the 2 θ range of 10° - 80° with a scan speed of 2°/min and a step size of 0.02°. The morphological observation and chemical composition analysis of the PEO-coated specimens, including the free surface, the fractured cross section and the coating/substrate interface of the stripped PEO coatings, were conducted using scanning electron microscopy (SEM, S-4800, Hitachi, Japan) assisted by energy dispersive spectrometer (EDS). Before SEM inspection, all PEO coatings were sputtered with a thin conductive gold film. During SEM examination and EDS detection, the instrument was utilized under an acceleration voltage of 15 kV and 20 kV, respectively, accompanied by a respective work distance of 10 mm and 15 mm. The 3-dimensional profiles of the coating surfaces were investigated using a laser scanning confocal microscope (LSCM, Zeiss LSM800, German), and

the 3D surface roughness values (areal arithmetic mean height, S_a) of the coatings were assessed according to the related 3D profiles. The weight gains of the PEO-coated specimens were evaluated using an analytical balance with a resolution of 10^{-4} g (BSA124S, Sartorius, German). Before mass measurements, the coated specimens were dried in a vacuum drying oven at 60°C for 12 h [37]. The thicknesses of the resulting coatings were assessed based on the fractured cross-sectional SEM micrographs of the stripped coatings at low magnification based on the calculation with Image Pro Plus 5.0 software (IPP, version 5.0, Media Cybernetics, USA). Thirty measurements of each specimen were carried out to obtain the average value. The sizes of the typical microstructures on/in the PEO coatings, such as sealed-hole pancake-shaped features and unsealed holes in the centers of pancakes, were also measured Image-Pro Plus software in light of the associated SEM photos. During the characterizations, the sampling positions referred to the central areas of each specimen.

Potentiodynamic polarization tests were performed to investigate the corrosion performance of the uncoated aluminum foil and the PEO-coated specimens in a corrosive liquid of 3.5 wt.% NaCl at room temperature, using an electrochemical workstation (RST5200, Shiruisi, China). The conventional three-electrode system was adopted for the tests: the specimens acted as working electrodes (a round area of 1 cm^2 exposed to the corrosive medium), a saturated calomel electrode (SCE) served as reference electrode and a platinum electrode worked as counter electrode. The tests were recorded at a potential range of $-0.5 \sim +0.5\text{ V}$ Vs OCP with a scan rate of 1 mV/s , and an embedded software of the electrochemical workstation was applied to process the data of the potentiodynamic polarization curves. To ensure reproducibility, three parallel specimens were used in the potentiodynamic polarization tests.

3. RESULTS AND DISCUSSION

3.1. Voltage-time response

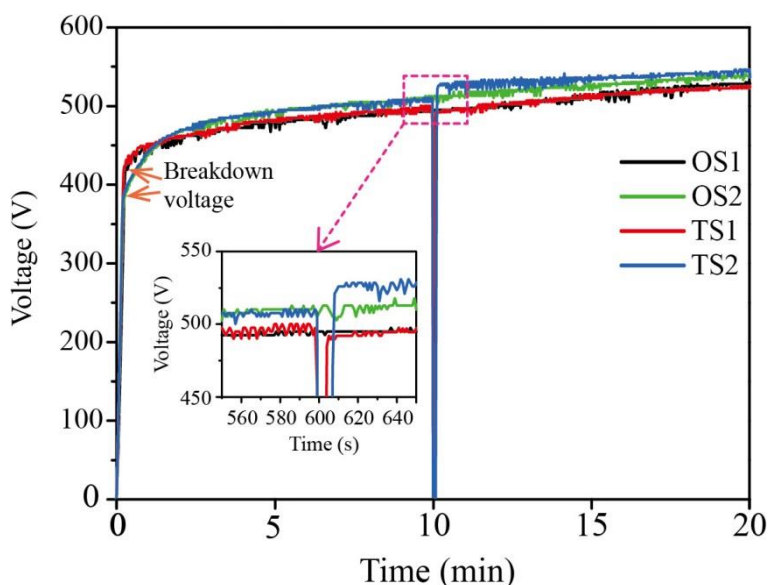


Figure 1. Voltage–time dependence of Al specimens galvanostatically processed under one-step and two-step PEO treatment regimes.

Table 3. Characteristic data acquired from the V-t plots in Fig. 1.

Specimen code	Breakdown voltage (V)	End voltage of first PEO step (V)	Initial voltage of second PEO step (V)	Final voltage (V)
P1	~ 421	—	—	~495
P2	~ 376	—	—	~513
OS1	~ 421	—	—	~531
OS2	~ 376	—	—	~540
TS1	—	~498	~485	~525
TS2	—	~510	~521	~546

The typical voltage responses with respect to time for aluminum specimens processed by one-step and two-step PEO treatment regimes are presented in Fig. 1, and the associated characteristic parameters extracted from Fig. 1 are listed in Table 3.

The voltage-time curves for a 20-min PEO treatment can be roughly divided into two parts based on the inflection point, named the breakdown voltage, and this sudden deflection of the V-t slope is linked to the commencement of fine discharge sparks related to the electronic current [38]. The linear part of the curve before the breakdown voltage corresponds to the conventional anodizing stage of the PEO process. When the anodic film grown on the anode surface reaches its critical thickness and the externally applied voltage increases to its threshold value of breakdown, the dielectric breakdown phenomenon of the anodic film and plasma microdischarges occur. As seen in Table 3, the breakdown voltages of anodic films in the cases of OS1 and OS2 collected in Si and SiW electrolytes are ~421 V and ~376 V, respectively, meaning that the additional presence of tungstate in the basic Si solution reduces the breakdown voltage of the associated anodic film. According to the classic model of the electrical breakdown of anodic films proposed by Ikonopisov, the formula is expressed as follows [39]:

$$V_b = a_B + b_B \log\left(\frac{1}{\kappa}\right) \quad (1)$$

where V_b is the breakdown voltage, a_B and b_B are constant quantities for a given valve metal and electrolyte constituent, κ is the ionic conductivity of the electrolyte. Obviously, the value of the dielectric breakdown voltage of the initial anodic film decreases when the conductivity of the electrolyte concerned increases, which is ascribed to the acceleration in the incorporation rate of the primary electron current into the conduction band of the oxide [38]. The variation tendency of the breakdown voltage values for the anodic films grown in Si and SiW electrolytes is in conformance with the changing trend reflected by the above theoretical model (equation (1)), indicating that the addition of tungstate anions plays a significant role in altering the characteristics of the resulting anodic film.

After exceeding the breakdown inflection point, dielectric breakdowns happen, and large amounts of tiny discharge sparks appear on the specimen surface. The formation and growth of PEO coatings during sparking regimes, primarily driven by plasma microdischarges, is an extremely complex process [40]. However, it is certain that the PEO coating process proceeds because of the defects residing in these coatings characterized by dielectric properties, which provide relatively low impedance routes for the pass-through of the current flow and are a prerequisite to ensure the continuity of PEO treatment under the externally applied electric field [41]. It is assumed that the

dielectric behaviors of nonconductors, especially the insulating strength, are highly dependent upon the existing and generated defects [42]. From Fig. 1, it is noticeable that when the voltage is beyond the breakdown value, the voltage-time responses in Si and SiW electrolytes are different in these two one-step cases. In the two-step PEO processes, the interchange of electrolytes at the time of 10 min also leads to the alteration of the corresponding V-t curves. In the V-t curve of TS1, the end voltage at 10 min acquired first in Si media is ~ 498 V, and then the initial voltage of recovering the sparking discharges in SiW system slightly drops to ~ 485 V. For a reverse sequence, i.e., in the V-t curve of TS2, the end voltage of 10 min monitored first in SiW is ~ 510 V, and then upon commencement of the second PEO treatment in Si, the initial voltage of recovering microdischarges rises to ~ 521 V. For the final voltage, the relevant value of TS1 is lower than those of OS1 and OS2, while the final voltage of TS2 is greater than that of OS1 and OS2. The results of Ref. [32, 35] showed that when a PEO-coated specimen was introduced into another electrolyte possessing a relatively low conductivity, the corresponding initial voltage of recovering microdischarges acquired in the second PEO step was less than the end voltage of the first PEO step. In Ref. [43], the authors drew an opposite conclusion. Therefore, it would seem that the difference in electrolyte conductivity, which results in discrepancies of breakdown voltages in Si and SiW electrolytes, may not be the determining factor that influences the voltage-time response behavior in the stable PEO sparking stage after the interchange of the electrolytes. On one hand, variations in the characteristics of defects and hence the associated impedance of the deposited coatings during PEO progress are responsible for the foregoing changes in the time dependence of the voltage response [44]. It is acknowledged that the number of defects in the PEO coatings gradually decreases with prolonged oxidation time under galvanostatic conditions, possibly due to the healing effect of the subsequently generated coatings on the defects in the pre-existing coatings [45] and that plasma discharge events (B-type) show a strong preference for occurring in cascades at the well-defined positions of residual microstructural defects (possibly predominantly at the holes) [17], which will accordingly enhance the applied voltage to overcome the increasing impedance of the dielectric coatings with PEO time. On the other hand, the difference between the formation rate and the dissolution rate of the coating involved during the PEO procedure has a direct bearing on the changes of the voltage-time characteristic behavior. The growth of PEO coatings is related to the dynamic competition between the formation of the new coating and the dissolution of the already present coating [46]. The PEO coating thickens when the associated formation rate is larger than the dissolution rate, and the corresponding voltage-time response increases in the current-controlled mode; on the contrary, the PEO coating becomes thin and the applied voltage declines. If the two rates stay balanced, the coating thickness remains unaltered, and the applied voltage holds constant. No matter which aspect (defects in the coatings or the competition between the growth and dissolution of the coating) dominates, the different V-t behaviors collected herein can be essentially attributed to the variation and interchange of the working electrolytes, which can affect the plasma microdischarge characteristics and the nature of the resultant coatings.

3.2. Phase composition

Fig. 2 exhibits the X-ray diffraction patterns of the PEO-coated Al specimens under one-step and two-step PEO treatment regimes. The diffraction pattern of Al appears in each case, due to the relatively thin thicknesses and the porosities of the resulting PEO coatings. The γ - Al_2O_3 phase is detected in all the coatings. Elemental tungsten (W) is discerned in the coatings of P2 and OS2~TS2 involving in the SiW electrolyte in addition to γ - Al_2O_3 .

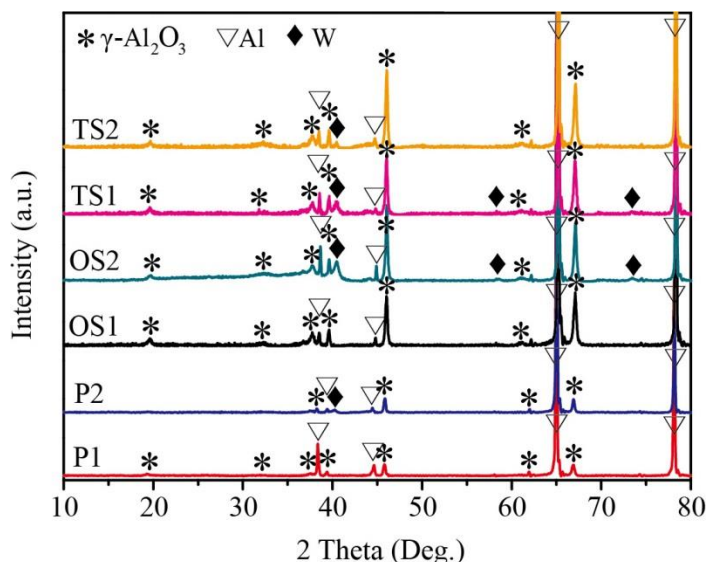
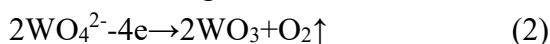


Figure 2. X-ray diffraction pattern of PEO-coated Al specimens under one-step and two-step PEO treatment regimes.

The formation of tungsten-bearing species (element W in XRD spectra) in the PEO coatings of P2 and OS2-TS2 indicates that the tungstate in the SiW electrolyte participates in the PEO coating process, which shows a good consistency with the results previously reported in literature [4, 47]. By means of optical emission spectroscopy (OES) investigation, it is noticed that [48] the components of plasma formed during PEO progress are complex, comprised of many species issued from the substrate and the electrolyte. Stojadinovic and coauthors [8] detected the emission lines of species (like W I) from the bulk solution and the lines of species (such as Al I and Al II) from the substrate during PEO processing of Al foil in a simple tungstate electrolyte with a concentration of 16.493 g/l. Possible chemical reaction equations involved in the formation of W are listed as follows [49, 50]:

Under the high temperature and high pressure that originates from plasma microdischarges, the decomposition of WO_4^{2-} ions may occur inside the discharge channels (reaction (2)). This supply of tungstate ions for the occurrence of reaction (2) can be realized by diffusion and migration processes, since tungstate ions will transfer toward the coating/substrate interface through discharge channels in the presence of a strong electric field under anodic polarization:



Due to the presence of an abundance of aluminum inside the discharge channels, the following

reaction can occur as well:



Reaction (3) is an exothermic reaction, which will release a considerable amount of heat in local areas and lead to the activation of this reaction; hence, it features self-maintenance [47], bringing about the existence of elemental tungsten in the relevant PEO coatings as indicated by the XRD spectrum. The diffraction peaks of intermediate products (WO_3) involved in the two reactions above are absent in the XRD pattern of the PEO coatings of P2 and OS2-TS2, which may be attributed to the low concentration of tungstate added in the current research [50]. The less tungstate present in the electrolyte, the less tungsten trioxide is formed during the reaction (2). Consequently, the produced tungsten trioxide will be depleted via reaction (3) with abundant Al. Alternatively, the content of tungsten trioxide is not within the XRD resolution limit.

3.3. Weight gain

Fig. 3 presents the weight gains of PEO-coated Al specimens under one-step and two-step PEO treatment regimes. The final weight gain of a PEO coating mainly refers to the difference value between the incorporation of species from electrolyte (Si, W and O in this study) into coating and the loss of metal substrate (Al in this study) to the bulk solution. The results in Fig. 3 indicate that the contribution from the coating process is larger than the loss of the metal species. A previous study based on the solution analyses of inductive coupled plasma-atomic emission spectroscopy (ICP-AES) has demonstrated that [21] the substrate metals partly dissolve into the electrolyte and that the concentrations of the metallic species in the bulk solution increase with the extension of oxidation time.

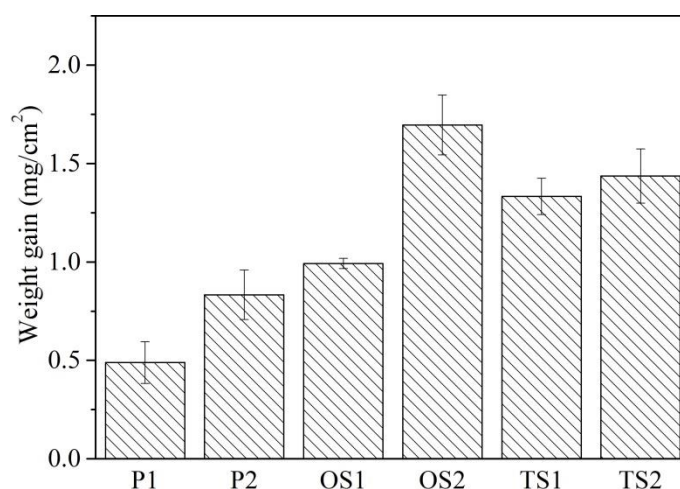


Figure 3. Weight gains of PEO-coated Al specimens under one-step and two-step PEO treatment regimes. Error bars indicate the standard deviation.

The test data from Fig. 3 shows that the order of the mean weight gains of the specimens is $P1 < P2 < OS1 < TS1 < TS2 < OS2$. The atomic mass of W is much larger than those of Si and O. The weight gain of P2 (OS2) is ~ 1.7 times that of P1 (OS1), suggesting the participation of tungstate in the PEO reaction and the incorporation of W-bearing species into the final coatings. OS2 has the highest weight gain among all specimens owing to the 20-min PEO treatment in SiW. The big difference in the weight gain between the two-step cases (TS1 and TS2) and one-step cases (OS1 and OS2) demonstrates that the two-step PEO treatment exerts an effect on the coating formation process. In the case of TS1, PEO is first performed in Si for 10 min and then in SiW for another 10 min, which means that the initial W-free coating materials generated in Si are partly dissolved and replaced by W-containing materials in SiW. In the case of TS2, the dissolution and replacement of the coating materials is in contrast to that in the case of TS1. However, the value of TS2 is slightly bigger than that of TS1, which is correlated with the faster growth rate and the greater thickness of TS2 in comparison to those of TS1 (see results in Section 3.5).

3.4. Surface morphology

Fig. 4 discloses the SEM micrographs of the surface morphology of the different PEO coatings prepared by one-step and two-step PEO treatment regimes.

All the surfaces exhibit characteristics of Al-based PEO coatings after being treated in alkaline silicate-based solution, namely, considerable deeply-colored pancake-shaped structures together with the surrounding light nodular features dominating the surfaces. The pancakes on the primary coating surfaces of P1 (Fig. 4a) and P2 (Fig. 4b) are predominantly unsealed-hole types. On P1's surface, circular-hole pancakes are the dominant type of open-hole pancakes. In the case of P2, some elongated-hole pancakes emerge, and the population of the elongated-hole pancakes is almost comparable to that of circular-hole pancakes on the whole, both of which are larger in dimension than those of P1. As the oxidation time lengthens, the previously formed open-hole pancakes at 10 min basically evolve into sealed-type pancakes on the surfaces of the OS1 (Fig. 4c) and OS2 (Fig. 4d), and the sealed-hole pancakes on OS2 usually possess larger average diameters than those on OS1. The surface morphologies of TS1 (Fig. 4e) and TS2 (Fig. 4f) are not exactly the same as those displayed by OS1 and OS2, respectively, although they are conducted for the same PEO time (20 min). Including the sealed-hole pancakes, the coating surfaces of TS1 and TS2 are sporadically speckled with some open-hole pancakes, which are similar to those typically present on P1 and P2, respectively. On TS1, the open-hole pancakes are mainly circular-hole type, while in the case of TS2, the elongated-hole and circular-hole types are almost equivalent in quantity. In other words, TS1 and TS2 additionally reveal morphologies similar to the primary coatings obtained in the first PEO step, i.e., P1 and P2, respectively. It follows that the initially synthesized PEO coatings partially control the morphology of the two-step processed coatings. In addition, apparent microcracks show up on the coating surfaces of OS1-TS2 (Fig. 4c-f), which radiate in the radial direction from the centers of the sealed and half-sealed pancakes, while few microcracks are present on P1 (Fig. 4a) and P2 (Fig. 4b) with unsealed pancakes.

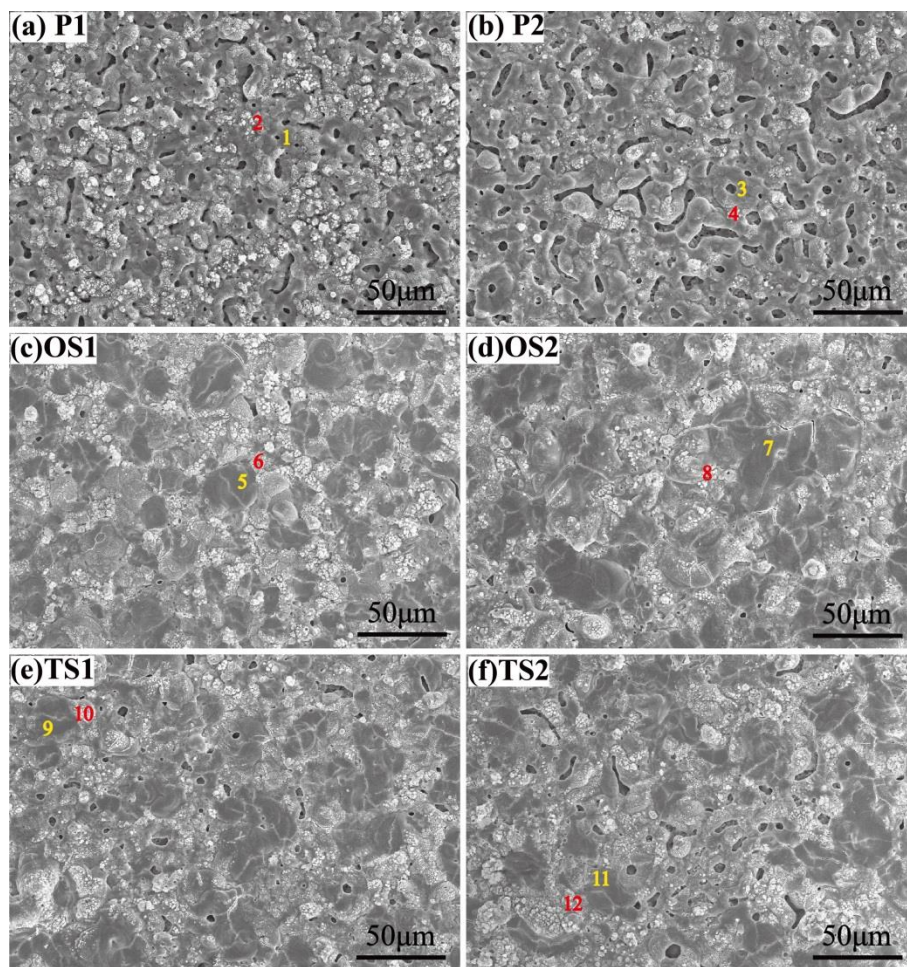


Figure 4. Surface SEM morphology of different Al-based PEO coatings processed via one-step and two-step treatment regimes.

Table 4. Surface component analysis of Al, O, Si and W elements at different study points in Fig. 4.

Specimen code	Study point	Element (wt.%)			
		Al	O	Si	W
P1	1	64.8	34.9	0.3	—
	2	27.4	47.0	25.6	—
P2	3	55.1	40.5	2.3	2.1
	4	32.6	40.1	15.4	11.9
OS1	5	51.0	41.6	7.4	—
	6	17.0	54.6	28.4	—
OS2	7	47.1	40.9	5.1	6.9
	8	9.3	44.0	20.4	26.3
TS1	9	52.9	39.9	3.1	4.1
	10	16.9	49.7	16.9	16.5
TS2	11	68.4	22.6	5.5	3.5
	12	14.7	49.4	25.6	10.3

Note: Points with odd numbers (yellow) are located in the pancake structures, while points with even numbers (red) are situated at the nodular features.

Notably, it can be seen from the EDS results (Table 4) that the pancakes on the surfaces of P1 and OS1 are rich in Al and O element, while the nodules around the pancakes are Si-enrich, which is in compliance with the result in another study [7]. In the cases of the remaining coatings (P2, OS2, TS1 and TS2) involving in the treatment in SiW, similar to the cases for P1 and TS1, the same distribution of Al, O and Si appears on the surfaces of these coatings. Also, W enrichment is observed on the nodules surrounding the pancakes on these coatings, which is basically the same as the enrichment of Si and confirms that tungstate is incorporated into the formed coatings. In conclusion, W and Si have the same distribution patterns on the coating surfaces.

Fig. 5 gives the three-dimensional surface profiles of the PEO coatings synthesized via one-step and two-step treatment regimes. Apparent mountain- and valley-like contours can be observed on each 3D-image of the coating surface, which are in close connection with the pancakes, nodules and even microcracks on the coating surfaces. The results here are basically in accordance with those revealed in Fig. 4.

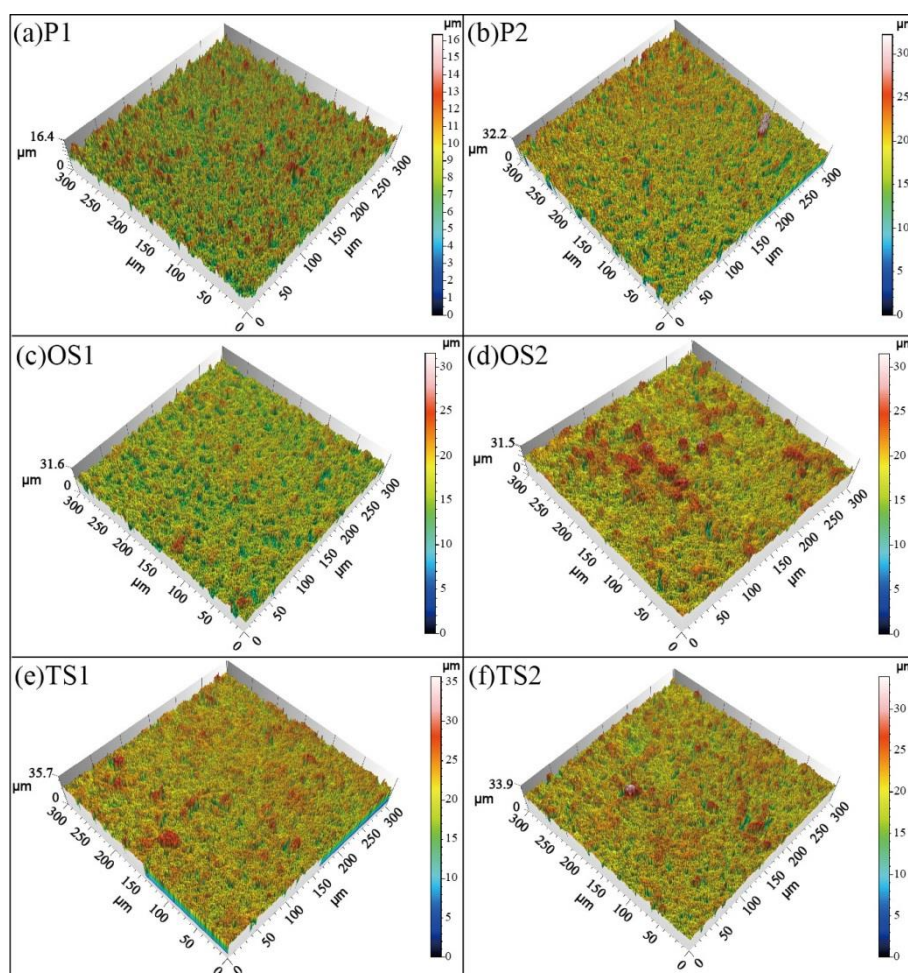


Figure 5. Three-dimensional surface morphologies of the PEO coatings synthesized via one-step and two-step treatment regimes.

Fig. 6 shows the areal arithmetic mean height (S_a) of the PEO coatings synthesized via one-step and two-step treatment regimes. S_a is the extension of R_a (the arithmetical mean height of a line) to a

surface. It expresses, as an absolute value, the difference in the height of each point compared to the arithmetical mean of the surface, which works better than R_a in evaluating the surface roughness. As evident in Fig. 6, P2 has the largest S_a value among all cases, which is highly relevant to the elongated-hole pancakes. TS2 possesses a slightly larger S_a value than TS1 due to the additional presence of elongated holes. The S_a value of OS2 is less than that of OS1, and it can be explained by more heat and oxygen formed in SiW than in Si (see equations in Section 3.2), both of which can promote the smooth flow of molten oxide with a larger volume over the surface.

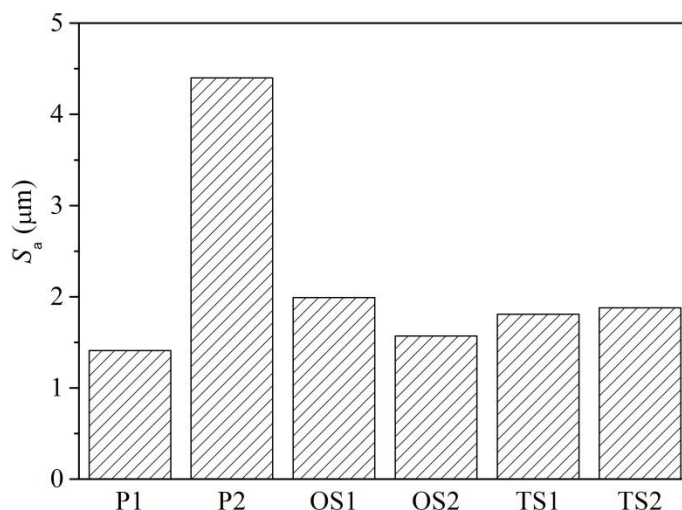


Figure 6. Areal arithmetic mean height (S_a) of the PEO coatings synthesized via one-step and two-step treatment regimes.

3.5. Fractured cross-sectional morphology of stripped PEO coatings

Fig. 7 illustrates the fractured cross-sectional micrographs of the stripped PEO coatings under one-step and two-step PEO treatment regimes, which reveals the characteristic features correspondingly observed in the surface morphology (Fig. 4) in each case. Measured based on the relatively low-magnification micrographs (Fig. 7a, c, e, g, i and l), the average coating thicknesses of P1-TS2 are $3.78 \pm 0.79 \mu\text{m}$, $7.71 \pm 2.15 \mu\text{m}$, $10.58 \pm 2.70 \mu\text{m}$, $17.82 \pm 4.52 \mu\text{m}$, $11.48 \pm 2.69 \mu\text{m}$ and $12.26 \pm 2.82 \mu\text{m}$, respectively, and the order of the average thicknesses is $P1 < P2 < OS1 < TS1 < TS2 < OS2$. In the one-step PEO cases, the contrast of the thicknesses between P1 (OS1) and P2 (OS2) shows that the average growth rates of the PEO coatings in SiW electrolyte are considerably improved, at roughly double what those obtained in Si solutions. Additionally, considering the average thicknesses of OS1-TS2 which are treated for 20 min, the two-step treatment does affect the coating growth rates during PEO. TS1 and TS2 are subjected to only 10-min treatment in SiW, and as a consequence, their final thicknesses are less than that of OS2 treated in SiW for 20 min. The thickness of TS2 is slightly greater than that of TS1, which is possibly ascribed to the slightly higher final voltage of TS2 with respect to that of TS1 (Fig. 1 and Table 3).

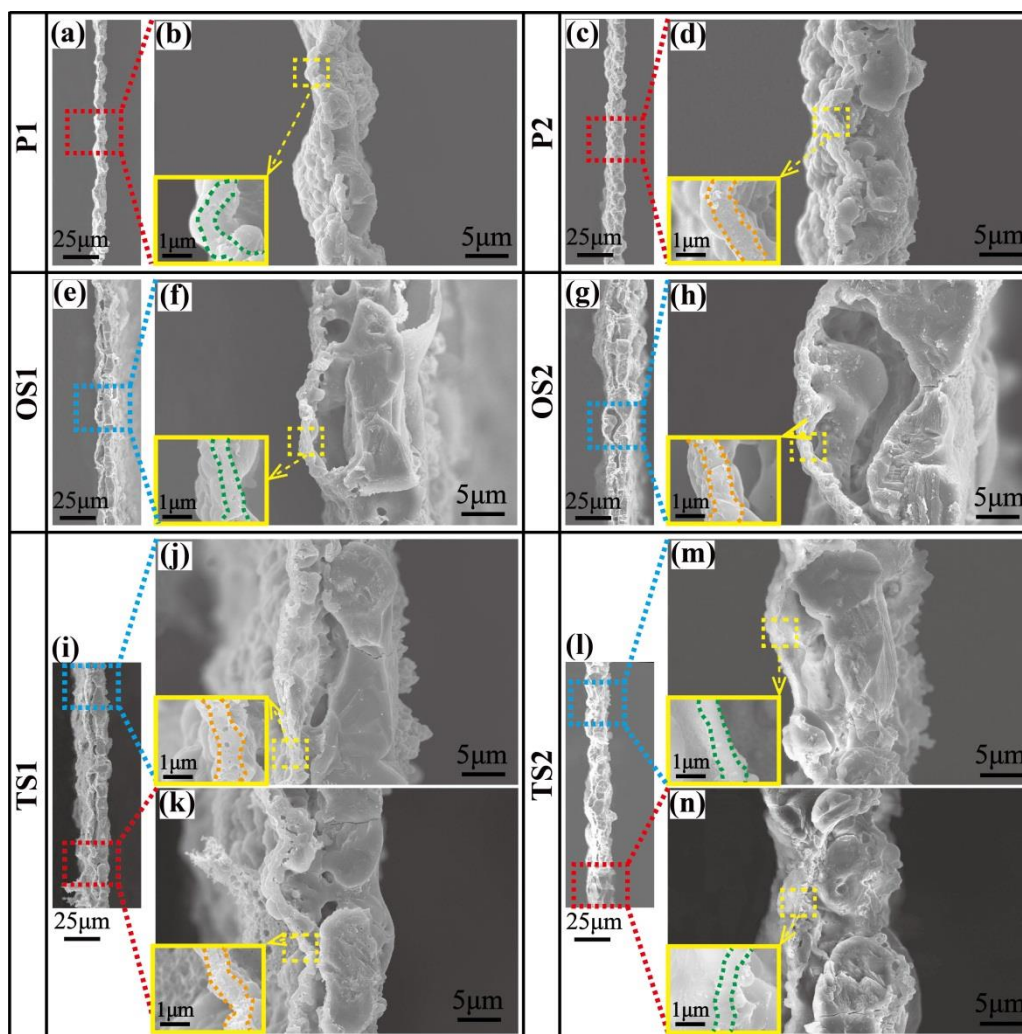


Figure 7. Fractured cross-sectional morphology of the stripped PEO coatings on Al synthesized by one-step and two-step treatment regimes. Note: red dotted rectangles refer to open-hole pancake structures, while blue ones refer to sealed pancakes. The yellow rectangles indicate the high-magnification view of the inner barrier layers.

From the magnified images of the fractured cross-sectional view, it is easy to find that all the PEO coatings exhibit distinct two-layered characteristics: thick and porous outer layers and comparably thin, compact inner barrier layers. Moreover, detailed coating structures are readily observed as follows: i) open-hole and/or sealed-hole pancakes in the outer layers (Fig. 7b, d, f, h, j, k, m and n); ii) cavities usually between the outer pancakes and the inner barrier layers (Fig. 7b, d, f, h, j, k, m and n); iii) isolated pores (submicron to micro-sized) resident within the outer layers (Fig. 7d, f and n); iv) microcracks passing through the cores of the sealed-hole pancakes (Fig. 7h and j) and v) even nodular structures present on the free surfaces surrounding the pancakes (Fig. 7f, j and n).

In addition, as illustrated in the insets of Fig. 7b, d, f and h, the average thicknesses of the inner barrier layers of both P2 and OS2 coatings ($\sim 0.76 \pm 0.07 \mu\text{m}$, $\sim 0.75 \pm 0.04 \mu\text{m}$) prepared in the SiW electrolyte are greater than those for both P1 and OS1 ($\sim 0.56 \pm 0.08 \mu\text{m}$, $\sim 0.54 \pm 0.08 \mu\text{m}$) in the Si media. The similar thicknesses between P1 and OS1, P2 and OS2, respectively, demonstrate that the thickness of the inner barrier layer in the PEO coating elaborated in the sparking regimes via one-step

PEO under certain treatment conditions (a given substrate, electrolyte, electrical parameters, etc.) remains approximately constant, independent of the treatment time. These rules show good consistency with the results reported in other researches [22, 28, 29]. Furthermore, the inset photos display that TS1 possesses a thicker inner barrier layer (with an average thickness of $\sim 0.75 \pm 0.08 \mu\text{m}$ in Fig. 7j and $\sim 0.75 \pm 0.06 \mu\text{m}$ in Fig. 7k) in comparison to that of TS2 ($\sim 0.56 \pm 0.05 \mu\text{m}$ in Fig. 7m and $\sim 0.55 \pm 0.04 \mu\text{m}$ in Fig. 7n). And the inset photos in Fig. 7 show that the thicknesses of the inner layers in TS1 and TS2 are basically equal to those of P2 (and OS2) and P1 (and OS1), respectively. These results indicate that the thicknesses of the inner barrier layers in the final coatings fabricated by two-step PEO treatments are determined by the second-step PEO, and further that the interchange of electrolytes in two-step PEO systems acclimatizes the primary coatings obtained in first-step to the second-step electrolyte systems. From the above findings, the order of the inner layer thicknesses among the six specimens is $(\text{P2} \approx \text{OS2} \approx \text{TS1}) > (\text{P1} \approx \text{OS1} \approx \text{TS2})$.

3.6. Corresponding relations among the coating/substrate interface, fractured cross-section and free surface morphologies

Fig. 8 displays the corresponding relations among the coating/substrate interface (L of Fig. 8), fractured cross-sectional (M of Fig. 8) and free surface morphologies (R of Fig. 8) of the PEO coatings elaborated under one-step and two-step PEO treatment regimes. For simplicity, the coating/substrate interface, fractured cross-section and free surface are referred to as C/SI, FCS and FS in this section, respectively.

Clearly, no sealed or unsealed pancakes, visible nodules or cracks appear on the C/SIs (L of Fig. 8), but some dome-like protrusions with different sizes are seen. From the integrated Fig. 8, it is easy to tell that the C/SI appearance is the contact surface between the thin dense inner barrier layer and the underlying Al substrate and that the protrusions belong to part of the C/SIs. Specifically, the corresponding relations among the above-mentioned structures can be summarized into two facets: a protrusion structure emerges in the C/SI (L of Fig. 8) and FCS (M of Fig. 8) micrographs, respectively, and a sealed-hole pancake and/or an open hole appears in the FCS (M of Fig. 8) and FS (R of Fig. 8) micrographs, respectively. These characteristic microstructures in the different micrographs basically have dimensional consistency (measured by IPP software, as given in Fig. 8). An obvious codependent relationship always exists among a protrusion in the C/SI, an open and/or a sealed-hole pancake in the outer layer and a cavity between the outer pancake and the inner barrier layer in PEO coatings. Apparently, the larger diameter of a sealed pancake or an open hole, the larger is the dimension of a protrusion formed along with a cavity.

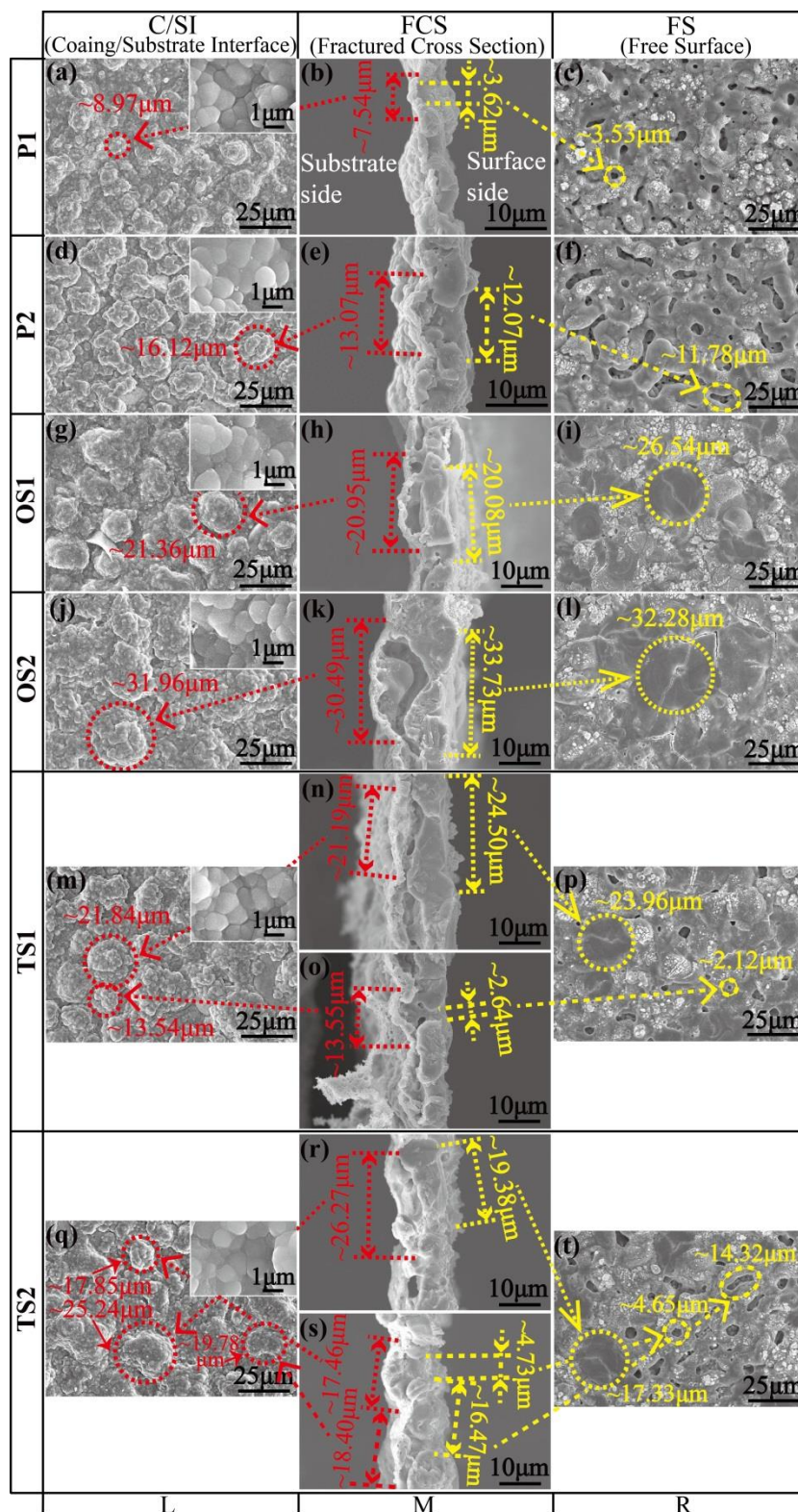


Figure 8. Corresponding relations among the coating/substrate interface (the left column, L), fractured cross-section (the middle column, M), the free surface morphologies (the right column, R) of the stripped PEO coatings synthesized via one-step and two-step treatment regimes.

From the open-hole pancakes in cases of P1-P2 (Fig. 8b-c, e-f) and TS1 and TS2 (Fig. 8o-p, s-t), it can be found that these holes have relatively smooth edges. Moreover, the core areas of the

sealed-hole pancakes in OS1-TS2 (Fig. 8h, k, n, r) are the thinnest region compared to the adjacent regions, and there is a natural thickening of the coating thickness from the cores to the borders of the sealed-hole pancakes along the radial direction. It is universally accepted that strong penetrating B-type discharges influenced by high electric field are primarily responsible for the formation of pancake-shaped features on PEO coating surfaces [7]. Combined with the codependence mentioned hereinbefore among the pancakes in the outer layers, the protrusions in the C/SIs and the cavities between the pancakes and the inner barrier layers, it can be concluded that the (open-hole or sealed-hole) pancakes together with the protrusions and cavities are caused by the synergistic effect among the dielectric breakdown of the coatings and the plasma discharges (B-type) from the coating/substrate interface, the generation and release of the gaseous products, and the formation, flowing and plastic deformation of the formed sticky coating materials. A distinct protrusion structure in the C/SI, which is directly contact with the Al substrate, definitely reflects that the PEO coating “devours” the metallic base, namely, it is a reflection of locally inhomogeneous inward growth of the PEO coating. These protruding areas, which were previously occupied by the base metal Al, are primarily consumed by energetic penetrating B-type sparking microdischarges to support the “expansion” of the PEO coatings toward the side of the underlying substrate under the effect of a high electric field [26, 28]. Therefore, it is more certain that the pancakes, together with the protrusions and cavities, arise from penetrating B-type discharges and that the dimensions of the characteristic features concerned can represent the discharge intensity to a certain degree during PEO. As can be observed from the C/SIs of the stripped PEO coatings (L of Fig. 8), the protrusions in the cases of OS1 (Fig. 8g) and OS2 (Fig. 8j) grew with the prolonged time and intensified discharges in comparison to those in P1 (Fig. 8a) and P2 (Fig. 8d), respectively. The protrusions in the cases of P2 and OS2 are larger than those in P1 and OS1, respectively. Compared with the cases of OS1 (Fig. 8g) and OS2 (Fig. 8j), both of which display the protrusions with relatively uniform sizes in each corresponding C/SI, the protrusions in the C/SIs of TS1 (Fig. 8m) and TS2 (Fig. 8q) are nonuniform in size affected by the extra typical features originating from their first-step PEO treatment, as revealed in P1 (Fig. 8a) and P2 (Fig. 8d). Furthermore, close examination of the protrusions in the C/SIs (insets of L in Fig. 8) reveals that there appear numerous collective micro-hemispheres which are basically of comparable average diameters: $0.92\pm 0.13\ \mu\text{m}$, $0.96\pm 0.13\ \mu\text{m}$, $0.93\pm 0.08\ \mu\text{m}$, $0.96\pm 0.14\ \mu\text{m}$, $0.95\pm 0.14\ \mu\text{m}$ and $0.93\pm 0.11\ \mu\text{m}$. Similar micro-hemispheres present in the C/SIs of Al-based PEO coatings have been reported in other works [21, 22, 24, 27, 28], which are closely linked with the sparking discharges penetrating through the thin interface layer between the coating and the substrate.

3.7. Growth models for PEO coatings fabricated via one-step and two-step treatment regimes

The growth models for the present PEO coatings synthesized via one-step and two-step PEO treatment regimes in Si and SiW electrolytes are proposed based on the foregoing characterization results and previous models [7, 21, 40]. The associated schematic illustration is depicted in Fig. 9.

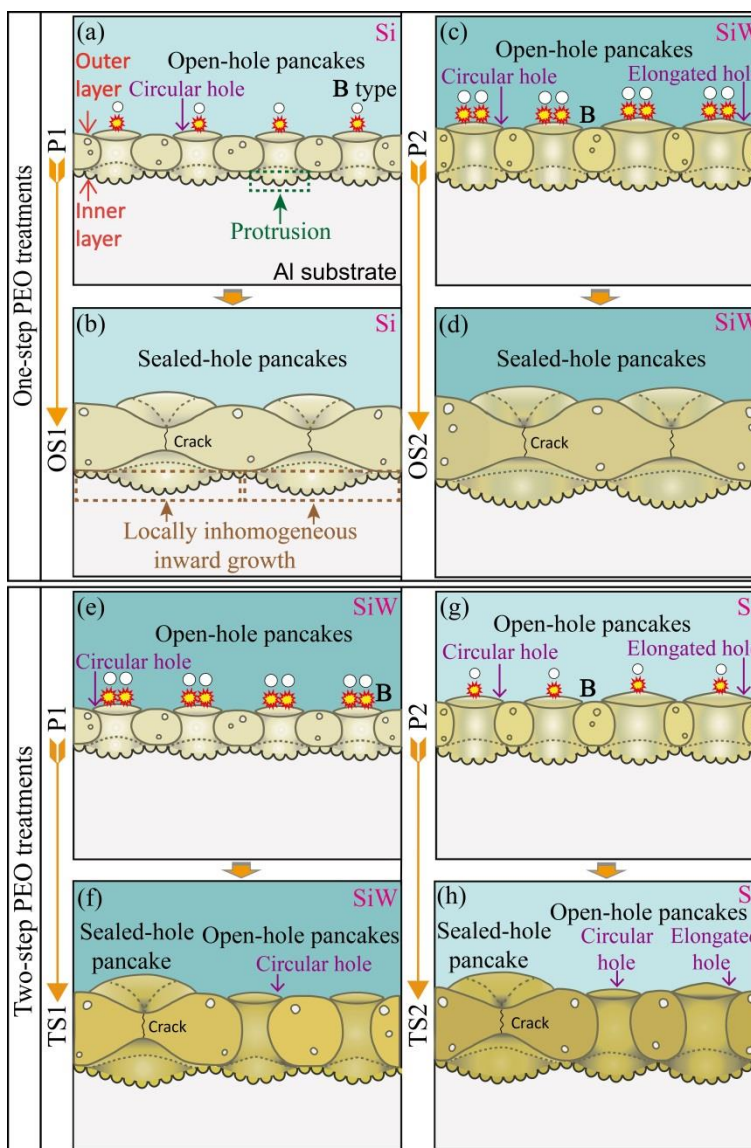


Figure 9. Schematic illustration of growth models for present PEO coatings fabricated via one-step and two-step treatment regimes.

In a strong electric field, the resulting coating materials, which are realized by reactions between the oxygen anions migrating from the bulk electrolyte and the aluminum cations from the substrate through dielectric breakdowns and plasma microdischarges, will be ejected from the central discharge channels, and then these materials will be solidified after they come into contact with the relatively cool electrolyte nearby, thus drawing the outline of pancake-shaped structures on the coating surface. In the interim, some relatively dispersed gas vapor products from the discharges are liable to build up and further be expelled along these channels, causing a repulsive force outward against the generated fused coating materials with a certain extent of plasticity. Generally, the central holes in the pancakes are the “footprints” of the discharge channels, and the development from central open holes to sealed holes depends mostly upon whether the integrative action of multiple influencing factors transforms from some kind of dynamic unbalance to a dynamic balance, which is determined by the energy and temperature of the plasma discharges, the volume and extrusion force of the released

gaseous phase products from the discharge sites, and the characteristics (volume, temperature, melting point and viscosity) of the produced fused coating materials [51, 52].

All the open-hole pancakes in the primary coatings of P1 and P2 originate from B-type discharges (Fig. 9a, c). At the treatment time of 10 min, the produced oxide melt stemming from the relatively soft microdischarges may be too “weak” (low melting point, less volume and lower fluidity) to flow back toward the originally formed discharge holes relative to the effect of extrusion force from the released gas from discharge sites, reaching some kind of dynamic unbalance in the formation of pancakes during PEO. Then, open-hole pancakes are created in the primary coatings of P1 (Fig. 9a) and P2 (Fig. 9c). Additionally, tungstate anions, which are inclined to be absorbed on the electrolyte/coating interface during PEO under the action of an electric field, will also behave as the centers of discharge impurities [49], multiplying the discharge sites on some level in the SiW electrolyte (P2) compared to PEO in the Si solution (P1) (Fig. 9a, c). Furthermore, the detection of elemental tungsten in XRD analysis in the case of P2 (Fig. 2) confirms the occurrence of reactions (2) and (3) (Section 3.2). Although the exothermic reaction (3) could provide extra formation heat to the P2 coating compared to that of P1 at this point, the greater voltage and higher discharge intensity (Fig. 1), together with more discharge centers in the immediate region and more internally formed gas products, are more conducive to the accumulation of gaseous phase, leading to more extrusion force applied to the external molten coating materials and hence the creation of bigger open-hole pancakes in P2 (Fig. 9c) compared to those in P1 (Fig. 9a). Additionally, the elongated-type holes in P2 (Fig. 9c) may be associated with simultaneous discharges triggered by tungstate anions, which possess close separation distances in the local domain.

Considering the finding of Troughton and coauthors [17], the open-hole pancakes in the primary coatings of P1 and P2 will render re-discharges accessible to sustain the PEO reactions in the following processes in the OS1 (Fig. 9a) and OS2 (Fig. 9c) cases, since these open-hole pancakes, which are less resistant in coating impedance with respect to neighboring areas, are the direct and effective routes to the transportation of species for subsequent discharges. As a result of the thickening coatings and the increased coating impedance with PEO time, the decreased weak sites within the coatings but enhanced B-type discharges will bring about fewer but larger pancakes than before (Fig. 9b and d) [8]. The enhanced discharges induced by increased voltage over time, on one hand, can facilitate heat accumulation in the coatings. On the other hand, they can promote the generation of molten materials possibly with high melting point, larger volume and higher fluidities, all of which are beneficial to the backflow of the generated molten materials toward the originally-formed central holes in the pancakes. At this moment (20 min), the effect of the reflux of the molten materials is equal to and/or greater than that of the gas emission on the external molten coatings, and hence, a type of dynamic balance is achieved in the formation of pancakes during PEO. Consequently, the pancakes at 10 min in both OS1 and OS2 cases morph into sealed-hole pancakes at 20 min (Fig. 9b, d). Additionally, both the higher discharge intensities of OS2 than those of OS1 and the exothermic reaction (3) could further contribute to the fluidity of the molten coating materials issued from the central discharge channels, resulting in larger pancakes in OS2 (Fig. 9d) than those in OS1 (Fig. 9b). Correspondingly, the larger protrusion in the coating/substrate interface and larger cavities between the outer and inner layers (Fig. 9c-d) will be generated in the case of OS2 in comparison to the case of

OS1. The larger the size of the protrusion appearing on the coating/substrate interface, the higher is the level of locally inhomogeneous inward growth happening to the overall PEO coating.

As noted in Section 3.3 (Fig. 4a, b, e, f), the primary coatings produced in the first-step PEO treatment do affect the microstructural structures after the second-step treatment. The circular and elongated holes in the primary coatings of P1 and P2 will act as the preferential positions for the succedent discharges in the TS1 (Fig. 9e) and TS2 cases (Fig. 9g). The succedent discharges rebuild the coatings through (partial and/or thorough) destruction and re-construction of the pre-existing coatings [13]. As explained above, the generation of pancakes results from the integrative action of the plasma discharges, the released gas products and the produced fused coating materials. Moreover, as for the formation of open-hole or sealed-hole pancakes, it is constrained by the state of the dynamic unbalance or dynamic balance owing to the characteristics of the three aforementioned affecting factors. In the case of TS1, the existence of a few open-hole pancakes may be linked to the smaller final voltage of TS1 compared to those of OS1-OS2 and to more internally-formed gas caused by the increased discharge centers in the second media of SiW (equation (2)) compared to the first media of Si. The effect of destruction and reconstruction arising from the succedent penetrating discharges in certain regions of the second-step PEO on the open-hole pancakes derived from the first step (P1) could still be in dynamic unbalance during the formation of pancakes, eventually yielding open-hole pancakes in the second step in TS1. With regard to TS2, there are no more gas products and formation heat created in the second step in Si solution compared to those in SiW. Besides, the presence of some open elongated-hole pancakes from P1 will weaken the repair effect of the coating materials from subsequent penetrating discharges in the second step of TS2 and will further aggravate this dynamic unbalance during PEO, ultimately leaving several elongated-hole pancakes in the resulting coating of TS2, although the final voltage of TS2 is bigger than those of OS1-OS2 and TS1, respectively.

3.8. Corrosion resistance

The potentiodynamic polarization curves of the uncoated and coated Al specimens tested after being immersed in 3.5% NaCl for 0.5 h are shown in Fig. 10, and the associated electrochemical parameters extracted from these curves are summarized in Table 5. As the main characteristic parameters, the corrosion potentials (E_{corr}) and corrosion current densities (i_{corr}) are often used to evaluate the corrosion resistance of specimens [53]. The higher E_{corr} and the lower i_{corr} , the better is the resistance to corrosion of a specimen. The results in Table 5 denote that the bare Al specimen possesses the lowest E_{corr} and the highest i_{corr} , while for the PEO-coated specimens, the E_{corr} values shift in the positive direction and the i_{corr} values simultaneously move toward the negative direction with respect to those of the bare Al, which demonstrate that PEO coatings on Al result in improvement of the corrosion resistance ability.

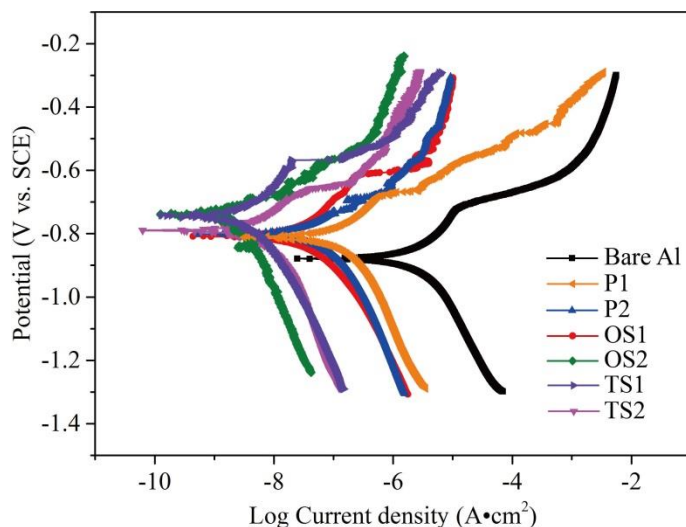


Figure 10. Potentiodynamic polarization curves of the uncoated and coated Al specimens tested after being immersed in 3.5% NaCl for 0.5 h.

Table 5. Electrochemical parameters extracted from potentiodynamic polarization curves.

	Bare Al	P1	P2	OS1	OS2	TS1	TS2
E_{corr} (V vs. SCE)	-0.88	-0.83	-0.80	-0.81	-0.74	-0.75	-0.79
i_{corr} (A/cm^2)	1.76×10^{-6}	1.09×10^{-7}	1.58×10^{-8}	2.27×10^{-8}	2.70×10^{-9}	2.95×10^{-9}	3.76×10^{-9}

Among all PEO-coated specimens, OS2 has the best corrosion resistance, and P1 shows the worst anti-corrosion property. The ranking order of the corrosion resistance for PEO specimens is OS2>TS1>TS2>P2>OS1>P1. In a study by Nabavi and coauthors [31], the results also show that not all two-step PEO coatings yield better anti-corrosion properties than do the one-step coatings. Thus, it can be seen that the corrosion resistance of two-step coatings is essentially influenced by the electrolytes and electrical parameters (such as time and treatment mode) applied in both the first and second PEO steps. It is generally held that the corrosion resistance of a PEO coating is determined by many factors (phase, the morphology and thickness of the inner barrier layer, etc.) [31, 38]. In the present PEO coatings, the significance of three aspects need to be considered in evaluating anti-corrosion properties: i) the elemental tungsten in the PEO coatings created in the SiW electrolyte could build protective barriers to inhibit the transportation of oxygen and chloride ions; ii) compared with open-hole pancakes, sealed-hole pancake structures play a role in preventing the direct access of aggressive media into the coating/substrate interface to some extent; iii) the relatively dense inner barrier layers of the PEO coatings, rather than porous outer layers, often provide the main protection function in anti-corrosion when only the thickness is considered, so PEO specimens with thicker inner barrier layers are more resistant to corrosion than those are with thinner inner barrier layers. OS2 has the above advantages compared to the other PEO specimens, thus offering the best anti-corrosion performance. In contrast, P1 performs the worst in resistance to corrosion due to lacking these advantages.

4. CONCLUSIONS

PEO processing of Al is galvanostatically conducted through one-step and two-step treatment regimes in an alkaline silicate electrolyte doped without and with tungstate. The microstructure investigations indicate that the thicknesses of the inner barrier layers in the final coatings elaborated via two-step PEO treatments are determined by the second-step PEO processing. Moreover, a one-to-one corresponding relationship exists between a pancake in the outer layer and a protrusion in the coating/substrate interface. The larger the average diameters of the sealed pancakes or open holes, the larger are the dimensions of the protrusions in the inner layers and the concomitant cavities between the outer and inner layers. Furthermore, growth models of the present PEO coatings are established based on the fact that the structures in the primary coatings prepared in the first-step PEO affect the final structures obtained after the second-step PEO. Open-hole pancakes in the primary coatings provide preferential access to reoccurrence of the penetrating discharges (B-type) during the follow-up PEO process. Finally, the one-step PEO coating treated in mixed silicate-tungstate electrolyte for 20 min possesses the best corrosion resistance with respect to the bare Al and other PEO coatings, owing to the presence of elemental tungsten, sealed-hole pancakes, and a relatively thicker inner barrier layer in the coating.

ACKNOWLEDGEMENTS

This work was supported by National Natural Science Foundation of China (Nos. 51671167 and 51171167) and Natural Science Foundation of Hebei Province, China (Nos. 2015203348 and B2015203406).

References

1. B.L. Pereira, C.M. Lepienski, I. Mazzaro and N.K. Kuromoto, *Mater. Sci. Eng. C: Mater.*, 77 (2017) 1235.
2. Y. Zhang, W. Fan, H.Q. Du and Y.W. Zhao, *Int. J. Electrochem. Sci.*, 12 (2017) 6788.
3. R.O. Hussein, X. Nie and D.O. Northwood, *Surf. Coat. Technol.*, 205 (2010) 1659.
4. T. Arunnellaiappan, L.R. Krishna, S. Anoop, R.U. Rani and N. Rameshbabu, *Surf. Coat. Technol.*, 307 (2016) 735.
5. R. Liu, J. Wu, W. Xue, Y. Qu, C. Yang, B. Wang and X. Wu, *Mater. Chem. Phys.*, 148 (2014) 284.
6. W. Zhang, B. Tian, K.Q. Du, H.X. Zhang and F.H. Wang, *Int. J. Electrochem. Sci.*, 6 (2011) 5228.
7. R.O. Hussein, X. Nie, D.O. Northwood, A. Yerokhin and A. Matthews, *J. Phys. D: Appl. Phys.*, 43 (2010) 105203.
8. S. Stojadinovic, R. Vasilic, I. Belca, M. Petkovic, B. Kasalica, Z. Nedic and L. Zekovic, *Corros. Sci.*, 52 (2010) 3258.
9. M. Boinet, S. Verdier, S. Maximovitch and F. Dalard, *Surf. Coat. Technol.*, 199 (2005) 141.
10. A. Yerokhin, E.V. Parfenov, C.J. Liang, V.R. Mukaeva and A. Matthews, *Electrochem. Commun.*, 27 (2013) 137.
11. D. Veys-Renaux, E. Rocca and G. Henrion, *Electrochem. Commun.*, 31 (2013) 42.
12. E. Matykina, R. Arrabal, D.J. Scurr, A. Baron, P. Skeldon and G.E. Thompson, *Corros. Sci.*, 52 (2010) 1070.
13. X. Liu, G. Li and Y. Xia, *Surf. Coat. Technol.*, 206 (2012) 4462.
14. S. Moon, R. Arrabal and E. Matykina, *Mater. Lett.*, 161 (2015) 439.
15. E.K. Tillous, T. Toll-Duchanoy and E. Bauer-Grosse, *Surf. Coat. Technol.*, 203 (2009) 1850.

16. X. Zhang, S. Aliasghari, A. Němcová, T. Burnett, I. Kuběna, Š.M, G. Thompson, P. Skeldon and P. Withers, *ACS Appl. Mater. Inter.*, 8 (2016) 8801.
17. S.C. Troughton, A. Nominé, J. Dean and T.W. Clyne, *Appl. Surf. Sci.*, 389 (2016) 260.
18. X. Lu, C. Blawert, D. Tolnai, T. Subroto, K.U. Kainer, T. Zhang, F. Wang and M.L. Zheludkevich, *Corros. Sci.*, 139 (2018) 395.
19. J.A. Curran and T.W. Clyne, *Surf. Coat. Technol.*, 199 (2005) 168.
20. K. Tillous, T. Toll-Duchanoy, E. Bauer-Grosse, L. Hericher and G. Geandier, *Surf. Coat. Technol.*, 203 (2009) 2969.
21. B. Kasalica, J. Radić-Perić, M. Perić, M. Petković-Benazzouz, I. Belča and M. Sarvan, *Surf. Coat. Technol.*, 298 (2016) 24.
22. C. Liu, D. He, Q. Yan, Z. Huang, P. Liu, D. Li, G. Jiang, H. Ma, P. Nash and D. Shen, *Surf. Coat. Technol.*, 280 (2015) 86.
23. C. Liu, P. Liu, Z. Huang, Q. Yan, R. Guo, D. Li, G. Jiang and D. Shen, *Surf. Coat. Technol.*, 286 (2016) 223.
24. Y. Zhang, Y.K. Wu, D. Chen, R.Q. Wang, D.L. Li, C.H. Guo, G.R. Jiang, D.J. Shen, S.X. Yu and P. Nash, *Surf. Coat. Technol.*, 321 (2017) 236.
25. R.Q. Wang, Y.K. Wu, G.R. Wu, D. Chen, D.L. He, D. Li, C. Guo, Y. Zhou, D. Shen and P. Nash, *J. Alloy. Compd.*, 753 (2018) 272.
26. Y.K. Wu, Z. Yang, R.Q. Wang, G.R. Wu, D. Chen, D.D. Wang, X.T. Liu, D.L. Li, C.H. Guo, S.X. Yu, D.J. Shen and P. Nash, *Surf. Coat. Technol.*, 351 (2018) 136.
27. M. Sabouri and S.M.M. Khoei, *Surf. Coat. Technol.*, 334 (2017) 543.
28. Y. Zou, Y. Wang, Z. Sun, Y. Cui, T. Jin, D. Wei, J. Ouyang, D. Jia and Y. Zhou, *Surf. Coat. Technol.*, 342 (2018) 198.
29. X. Liu, S. Wang, N. Du, X. Li and Q. Zhao, *Coatings*, 8 (2018) 105.
30. T. Zhan, W. Tu, Y. Cheng, J. Han, B. Su and Y. Cheng, *Ceram. Int.*, 44 (2018) 10402.
31. H.F. Nabavi, M. Aliofkhaezraei and A.S. Rouhaghdam, *Surf. Coat. Technol.*, 322 (2017) 59.
32. E. Matykina, G. Doucet, F. Monfort, A. Berkani, P. Skeldon, G.E. Thompson, *Electrochim. Acta*, 51 (2006) 4709.
33. W. Li, Z. Qian, X. Liu, L. Zhu and H. Liu, *Appl. Surf. Sci.*, 356 (2015) 581.
34. S. Tsunekawa, Y. Aoki and H. Habazaki, *Surf. Coat. Technol.*, 205 (2011) 4732.
35. A.M. Kumar, H.K. Sun, H.C. Jung and K.S. Shin, *Mater. Chem. Phys.*, 149-150 (2015) 480.
36. D.J. Shen, Y. Q and D.L. He, *CN: Patent* 2014102388007. 2016-06-15.
37. Y.H. Wang, Z.G. Liu, J.H. Ouyang, Y.M. Wang and Y. Zhou, *Appl. Surf. Sci.*, 258 (2012) 8946.
38. K. Venkateswarlu, N. Rameshbabu, D. Sreekanth, M. Sandhyarani, A.C. Bose, V. Muthupandi and S. Subramanian, *Electrochim. Acta*, 105 (2013) 468.
39. S. Ikonopisov, *Electrochim. Acta*, 22 (1977) 1077.
40. R.O. Hussein, X. Nie and D.O. Northwood, *Electrochim Acta*, 112 (2013) 111.
41. A. Ghasemi, V.S. Raja, C. Blawert, W. Dietzel and K.U. Kainer, *Surf. Coat. Technol.*, 204 (2010) 1469.
42. B. Kasalica, M. Petkovic, I. Belca, S. Stojadinovic and L. Zekovic, *Surf. Coat. Technol.*, 203 (2009) 3000.
43. R. Arrabal, E. Matykina, P. Skeldon, G.E. Thompson and A. Pardo, *J. Electrochem. Soc.*, 155 (2008) C101.
44. Y. Gao, A. Yerokhin, E. Parfenov and A. Matthews, *Electrochim. Acta*, 149 (2014) 218.
45. G. Sundararajan and L.R. Krishna, *Surf. Coat. Technol.*, 167 (2003) 269-277.
46. L. Chang, *J. Alloy. Compd.*, 468 (2009) 462-465.
47. A. Hakimizad, K. Raeissi, M. Santamaria and M. Asghari, *Electrochim. Acta*, 284 (2018) 618.
48. C.S. Dunleavy, I.O. Golosnoy, J.A. Curran and T.W. Clyne, *Surf. Coat. Technol.*, 203 (2009) 3410.
49. H.Y. Zheng, Y.K. Wang, B.S. Li and G.R. Han, *Mater. Lett.*, 59 (2005) 139.
50. C.C. Tseng, J.L. Lee, T.H. Kuo, S.N. Kuo and K.H. Tseng, *Surf. Coat. Technol.*, 206 (2012) 3437.

51. Y. Cheng, J. Cao, M. Mao, H. Xie and P. Skeldon, *Surf. Coat. Technol.*, 291 (2016) 239.
52. C. Blawert, S.P. Sah, J. Liang, Y. Huang and D. Höche, *Surf. Coat. Technol.*, 213 (2012) 48.
53. Y. Long, L. Wu, Z. Zhang, A. Atrens, F.S. Pan, A. Tang and G. Zhang, *Int. J. Electrochem. Sci.*, 13 (2018) 7157.

© 2019 The Authors. Published by ESG (www.electrochemsci.org). This article is an open access article distributed under the terms and conditions of the Creative Commons Attribution license (<http://creativecommons.org/licenses/by/4.0/>).